

HIGH RESOLUTION HST-COS Ly α PROFILE

C. SCARLATA, M. HAYES, L. COWIE AND ET AL.

Draft version August 27, 2013

ABSTRACT

Subject headings: galaxies: ISM — ISM: structure

1. INTRODUCTION

Ly α -based samples additionally carry the potential to constrain the epoch of cosmic reionization via an expected sharp drop in their number density as the ionization state of the intergalactic medium (IGM) changes (Miralda-Escudé & Rees 1998, Malhotra & Rhoads 2006). However, this interpretation hinges on a complete understanding of the Ly α escape physics, and on the evolution of the intrinsic properties of the Ly α emitter population as a function of redshift.

An ultraviolet resonant line such as Ly α is highly sensitive to the relative geometry and kinematics of the gas and dust, which is bound to change when subject to the dynamical effects of the increased merger rate with increasing redshift, as well as the varying and observationally undetermined H I content of galaxies. Most of our knowledge comes from small, non-representative samples of Ly α emitters at $z = 0$, and from cosmological populations of Ly α emitters ($z > 2$, for which the supplementary observations required to characterize galaxy physical properties, such as optical emission lines, are redshifted to expensive and/or inaccessible wavelengths). Therefore, a comprehensive study of the astrophysics behind the Ly α production, transport, and escape has not so far been made. This presents a fundamental limitation to our ability to use the Ly α emission as a cosmological tool.

We use a standard $H_0 = 70 \text{ km s}^{-1} \text{ Mpc}^{-1}$, $\Omega_M = 0.3$, and $\Omega_\Lambda = 0.7$ cosmology.

2. THE SAMPLE

The targets for the HST COS spectroscopic followup are taken from the sample of Ly α emitters identified by Deharveng et al. (2008) and Cowie et al. (2010) in deep GALEX grism spectroscopy. The GALEX sample includes 119 Ly α emitters, 49 of which have rest-frame Ly α emission line $\text{EW} > 20\text{\AA}$. From the parent sample of GALEX Ly α emitters, we originally selected 25 galax-

ies that satisfied the following criteria: 1) are classified as star-forming based on optical emission line ratios (e.g., Cowie et al. 2010), 2) have Ly α emission line rest-frame $\text{EW} > 20\text{\AA}$ in the low resolution GALEX spectra, and 3) have redshift confirmed using optical spectroscopy. As we show in Scarlata et al. (2009), Atek et al. (2009), Finkelstein et al. (2009), and Cowie et al. (2010), the requirement of having the optical confirmation does not change the target selection function of the sample, since 100% of the sources we followed up were, in fact, confirmed. High redshift Ly α emitters are usually selected with Hu et al.'s (1998) definition that they have a rest frame EW greater than 20\AA (see also Kornei et al. 2010). Thus, the EW cut ensures that we are able to make a valid comparison with the samples of Ly α emitters selected at $z > 2$.

3. OBSERVATIONS AND DATA ANALYSIS

The galaxies were observed between February and October 2011, with the COS FUV, medium-resolution G160 grating. Each galaxy was observed for 1 orbit. For 22 out of the 25 galaxies, the imaging target acquisition was performed on a star close to the science target (distance $\leq 2''$). The telescope was then offset to center the COS aperture on the science target. The offsets were computed from ground based images in most cases, while ACS HST imaging was used for the objects in the COSMOS field (see Table ??). In order to check the acquisition procedure, we obtained a direct NUV image after the telescope was shifted to the target position. The exposure times of the images vary between 80 and 200 seconds, depending on the GALEX NUV magnitude of the target. The remainder of each orbit was used for the spectroscopic observations in TIME-TAG mode, with typical exposure times of 2300s. We chose the grating central wavelength to ensure that the Ly α would not fall in the wavelength gaps due to the physical layout of the detectors and the optics. In order to reduce the impact of microchannel plate detector fixed pattern noise, we took two exposures for each target, with FP-POS= 3 and FP-POS= 4, respectively. The wavelength range covered by the COS spectra is approximately $1405 - 1775\text{\AA}$, with a dispersion of $12.23 \text{ m\AA px}^{-1}$.

We calibrated and extracted the COS spectra using *calcos* v2.15.4 task in *pyraf*. Due to the target acquisition strategy, the galaxies were not perfectly centered in the COS aperture. We used the direct NUV images of the targets to measure the shifts in the dispersion direction between the position of the center of each galaxy and the expected position of the COS aperture center. The shifts ranged between -19 and 10 NUV pixels, with a standard deviation of 8 pixels (corresponding to 0.1\AA). The cor-

² Space Telescope Science Institute, 3700 San Martin Drive, Baltimore, MD 21218, USA

³ Observatoire de Geneve, 51, Ch. des Maillettes, CH-1290, Sauverny, Switzerland

⁴ California Institute of Technology, MS 105-24, Pasadena, CA 91125

⁵ Max-Planck-Institut für extraterrestrische Physik, Giessenbachstrasse 1, 85748 Garching, Germany

⁶ Research School of Astronomy and Astrophysics, the Australian National University, Canberra 0200, Australia

⁷ INAF/Osservatorio Astrofisico di Catania, Via S.Sofia 78, I-95123 Catania, Italy

⁸ Department of Astronomy, University of Padova, Vicolo dell'Osservatorio 3, I-35122, Padova, Italy

⁹ Supernova Ltd., Olde Yard Village 131, Northsound Road, Virgin Gorda, British Virgin Islands

rection to the wavelength zero point was applied to the wavelength column in the `corrtag` files, and `calcos` was the run again with the edited files as input. This correction does not only take care of the wavelength zero point, but also allows us to apply the proper sensitivity at each wavelength.

The PSA aperture throughput decreases toward the edges of the field of view, due to the increasing vignetting of the flux. This change in throughput is not accounted for in the `calcos` pipeline, which is optimized for point sources, and results in an underestimate of the extracted flux for extended sources. We scaled the extracted spectra by a correction factor computed using the directing imaging, and assuming that the aperture throughput is symmetric with respect to the aperture center. The scaling factors vary between 1.0 and 1.6. Because of the acquisition strategy, the vignetting correction may be significant even for very compact sources, if the object did not end up at the center of the aperture.

For four galaxies (see Table ??) the star used for the acquisition was too bright to be observed with MIRRORA. In these cases we performed the acquisition using MIRRORB and changed to MIRRORA for the science exposures. Although the change from MIRRORB to MIRRORA does not affect a target's relative location in the aperture, it does move the location of the aperture on the detector, making it impossible to measure the precise target's location in the aperture, even if a direct image was obtained after the shift. Because the zero point of the wavelength calibration depends on the position of the galaxy in the aperture, for these four galaxies we added a systematic error component to the wavelength calibration, equal to the standard deviation of the galaxies' centers in the dispersion direction (0.1Å, c.f.t. above).

In Figure 1 (left panel) we compare the total aperture-corrected NUV flux measured from the 2''5 COS aperture with the GALEX NUV total flux. For each galaxy, we show the COS measurements before and after vignetting correction, and the size of the points is proportional to the measurement of the half-light-radius (see below). The solid line indicates the 1:1 relation. The fluxes in the smaller COS apertures are systematically lower than the GALEX fluxes, indicating that the objects have substantial amount of UV light falling outside the COS aperture, with larger objects systematically deviating more from the 1:1 relation.

3.1. Measurement of line flux and wavelength of line peak

We show the Ly α profiles of the sample galaxies in Figure 5. The profiles are characterized by complex structure and asymmetric shape. For this reason, rather than fitting a single gaussian, we measure the total line flux by integrating the profile between $\pm 2.5\text{\AA}$ from the expected line center. We estimate the continuum by computing the median flux density within 2\AA on both sides of the line center. The line-flux error was computed from the error spectrum derived during the spectral extraction process.

For each galaxy, we also derived the wavelength corresponding to the peak(s) of the Ly α line profile, derived by fitting a Gaussian function to a small wavelength range ($\pm 0.6\text{\AA}$) centered around the visually identified position

of the peak. For the four objects for which MIRRORB was used in the acquisition process, errors in the peak wavelength include the 0.1\AA centering uncertainty. Hereafter we will use blue (red) peak, to identify the peak on the blue(red) side of the Ly α wavelength expected from the H α redshift. In Table ?? we report the total line flux, and the wavelength of the blue and red peaks.

3.2. Size measurement

We use the COS images to measure galaxies' sizes in the NUV. Because of the complicated morphology of the starforming regions in many of the galaxies, we cannot fit a smooth profile to the UV light distribution (e.g., GALEX0332-2811A). We have therefore computed the radius of the circular aperture containing half of the total NUV flux, using a curve of growth analysis. The centers used for the circular apertures are indicated with a cross in Figure 2. Because of the small aperture of the COS instrument, we use the GALEX NUV luminosity as an estimate of the total light of the galaxy⁹. Before computing the aperture flux, we multiplied each NUV image by the COS aperture response map to account for the decreasing throughput as function of the spatial offset from the aperture center (?). The half-light-radii are reported in Table ??.

4. RESULTS

4.1. UV-morphology

Being sensitive to light between 1600 and 3100Å, the COS NUV channel probes the continuum coming from hot young stars. Ly α is inside the NUV bandpass for only three of our galaxies, (those at $z > 0.31$), where the EW is anyway insufficient to dominate the global light, but could in principle extend the morphologies somewhat. Figure 2 we show the NUV COS images of the 25 galaxies, together with the position of the circular COS aperture (when it could be determined, see section 3). The galaxies show a variety of morphology in the NUV: in some objects (e.g., GALEX1417+5305) the UV light is distributed smoothly over a large part of the COS aperture (i.e., diffuse objects), in others (e.g., GALEX1417+5228) the light is concentrated in a single compact star cluster (i.e., compact objects), while in others (e.g., GALEX1000+0157) the light is distributed in multiple clumps. The morphological classification is reported in Table 2.

In Figure 1 (right panel) we compare the total, aperture-corrected Ly α flux from the COS spectra, with the line intensity derived in ?. For the Ly α luminosity, we use the vignetting correction derived from the NUV images, as explained in Section 3. The comparison between the GALEX and COS measurements is informative, because the two instruments have different aperture size. The dashed lines in both panels indicates a factor of two difference in luminosity between the GALEX and COS measurements. It is interesting that for most of the galaxies the Ly α luminosity measured within the COS aperture is less than a factor of two fainter than the GALEX measurement, while the opposite is true for the

⁹ We have checked that for the typical NUV-I colors of our sources, the color term between the GALEX and COS magnitudes is negligible.

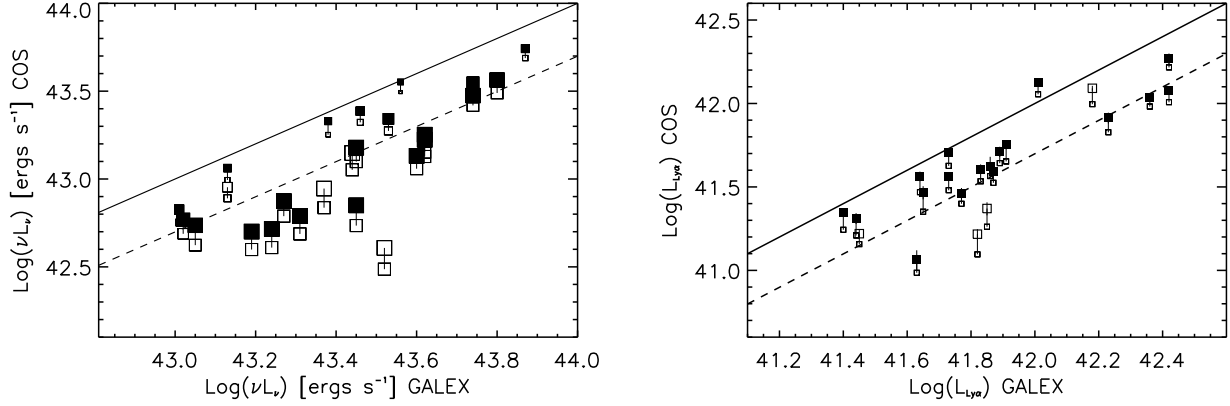


FIG. 1.— Comparison between the total luminosities as measured by GALEX and COS. The *Left* panel shows the continuum fluxes in monochromatic units, while the *Right* panel shows $\text{Ly}\alpha$. Large points have been corrected using the aperture correction estimated from the UV continuum. Open large squares indicate galaxies observed with MIRROR-B. After the aperture correction, approximately 30% of the $\text{Ly}\alpha$ flux is missed by the $2''.5$ COS aperture, indicating that the $\text{Ly}\alpha$ emission is more extended than the continuum.

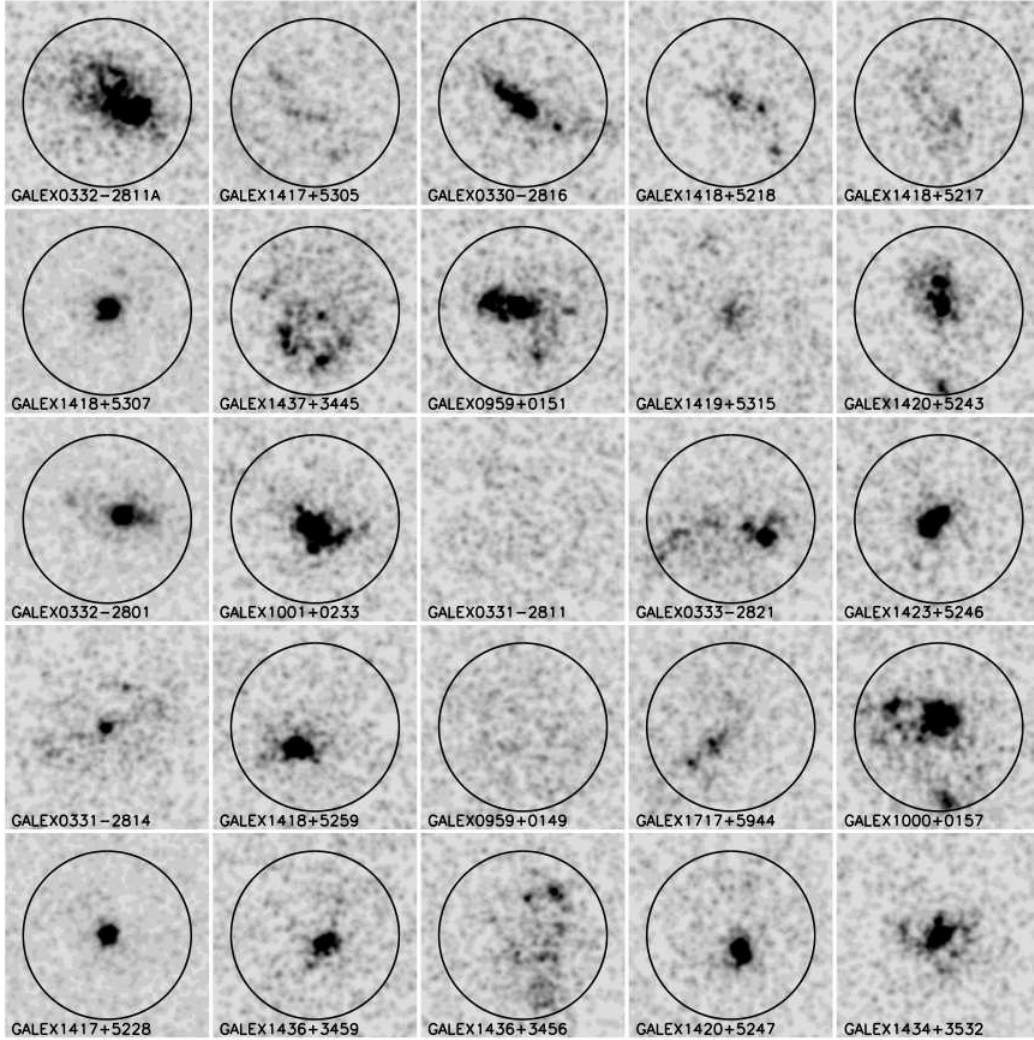


FIG. 2.— HST NUV images of the 25 sample galaxies observed with COS. The circle shows the position of the COS $2''.5$ aperture on the object. For four galaxies the position could not be determined (see text for detail).

UV luminosities. At face value, this result would indicate that the $\text{Ly}\alpha$ is more compact than the UV emission,

in contrast with the strong evidence for more extended $\text{Ly}\alpha$ -emission in nearby and high- z galaxies presented by

???, e.g., . Given the uncertainty in the vignetting corrections we do not discuss this point any further.

4.2. Ly α profiles

In Figure 3 we show the profiles of the Ly α emission lines, centered on the galaxy systemic velocity derived using the H α emission line. The spectra are shown after 8 pixels ($\sim 0.1\text{\AA}$) boxcar average. In two galaxies (GALEX1418+5259 and GALEX0959+0149) the Ly α line is very faint, and it is detected only after a rather heavy boxcar smoothing ($\sim 0.7\text{\AA}$). The vertical dashed line in each panel shows the expected wavelength position of the Ly α based on optical-lines redshift measurements. In a clear majority of cases (~ 20 of 25) the peak of the Ly α line is notably offset in wavelegnth to the red of the systemic velocity. In some cases multiple peaks are also visible, with a tendency (at least 10 cases) to show an additional peak on the blue side of the main peak, and also clearly bluewards of the systemic velocity. A handful of galaxies show additional red peaks that are clearly separated in three cases, and also extended bumps in the red wings of the primary line that could also be indicative of extended red features.

Using the measured wavelengths of the strongest Ly α emission peak, we compute the offsets relative to H α . These values are presented also in Table ?? and range generally between -50 and $+350$ km/s, with a mean velocity shift of 121 ± 18 km/s (standard error on the mean). We present this velocity distribution in the form of a histogram in Figure 4.

4.3. Continuum properties of the sample

The observations were designed to target the Ly α line, and consequently the continuum is not well exposed in individual galaxies. In Figure 5 we present the full COS spectra shifted into the rest-frame using the redshift measured from the H α emission line. The spectra are boxcar smoothed using a box of 1\AA , and are shifted in the vertical direction for clarity. The horizontal dashed lines show the zero flux level corresponding to each galaxy spectrum, while vertical lines mark the wavelength position of some prominent interstellar absorption features. Figure 5 shows that we are able to identify the strongest absorption feature only in a few individual sources, although the low S/N of the spectra prevent us from performing an accurate analysis.

Sample-averaged inferences can, however, be made through a stacking analysis. We blueshift the observed spectra into the rest-frame using the measured H α velocities. At every wavelength we compute a flux-weighted average and standard deviation. The mean stacked UV spectrum (shown after a box-car smoothing of 0.85\AA) can be seen in Figure 6, where the shaded gray area corresponds to the weighted standard deviation, and the top panel shows the number of galaxies that entered the stack at each wavelength.

We are able to identify and clearly measure the features presented in Table 1 and marked in Figure 6. The list includes five lines that form in the ISM and one (CIII λ 1175) that is mainly photospheric. It is reassuring that the velocity shift of the CIII photospheric line is consistent with zero, as would be expected for young massive stars responsible of the ionization of the HII regions. The ISM

TABLE 1
ABSORPTION LINES MEASURED IN THE STACKED SPECTRUM.

Species	Formation	λ_{vac} Å	λ_{obs} Å	ΔV
H I Ly α	ISM	1215.67	1216.09	104.30
C III	Photo	1175.53	1175.37	-39 ± 41
Si II	ISM	1190.42	1189.83	-159.97
Si II	ISM	1193.29	1192.60	-173.39
Si III	ISM	1206.50	1205.87	-156.02
Si II	ISM	1260.42	1259.56	-205.19
Si II	ISM	1304.37	1259.56	-205.19
C II	ISM	1334.53	1333.81	-161.69

lines, on the other hand, all show asymmetric absorption profiles, with the peak blueshifted outflow velocities in the range between $150\text{--}200$ km s $^{-1}$.

5. DISCUSSION

5.1. Ly α output and UV surface density

Smaller galaxies tend to have larger Ly α EW (Figure 7), however, this does not seem to be a consequence of smaller galaxies having a higher UV surface density (Figure 8) surface density.

6. SIMPLE MODEL FOR THE NEUTRAL GAS KINEMATICS

The stacked spectrum presented in Figure 6 shows a combination of blueshifted resonant absorptions and fluorescent emissions of [Si II] that can be used to constrain the kinematics and geometry of the neutral gas around the star-forming regions (e.g., ???).

We will start with the simplest description for the gas/star configuration, and approximate the galaxy as a spherical source of UV radiation with radius R_{SF} , surrounded by an expanding envelope of gas, extending to R_W . In the following we will refer to the expanding envelope as to the galactic wind. In Figure ?? we show the geometry of the wind and the definition of the coordinate system. We also define the radial coordinate in units of R_{SF} , $\rho = r/R_{SF}$.

It is well known that a spherical expanding envelope gives rise to a P Cyg -like profile due to line photon scattering. The theory of the formation of the P Cyg profile is well established **not the right word**, and we will discuss here only the main assumptions/ideas.

Looking at Figure ?? it is clear that only the wind material in front of the continuum source will produce an absorption feature in the spectrum by scattering out of the line of sight those photons with frequency corresponding to the resonant transition. Resonant photons, however, can be absorbed everywhere in the envelope, and will be re-emitted isotropically. Thus, at each *observed* velocity (i.e., the component of the velocity projected along the line of sight to the observer, $v_{\text{obs}} = v \cos \theta$), the transmitted flux will be the combination of both absorption and emission (i.e., scattered into the line of sight).

If the line optical depth $\tau_{\text{line}} \gg 1$, photons will interact with the outflowing material only where the absorbing ions are perfectly “at resonance” with those photons, due to their Doppler shift (condition also known as Sobolev’ approximation, ?). In this case, the radiative transport of the line photons can be reduced to a local problem, and the optical depth for absorption (τ) can

FIG. 3.— Rest-frame COS spectra of the 25 sample galaxies around the $\text{Ly}\alpha$ emission lines. The systemic velocity is determined from the nebular $\text{H}\alpha$ line. The spectra have been boxcar smoothed by 0.5\AA .

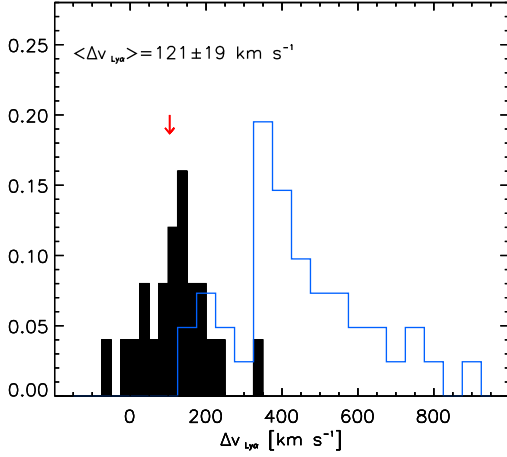


FIG. 4.— Histogram of the velocity difference between the Ly α and H α line. The black solid histogram shows the shifts for our GALEX LAEs at $z \approx 0.2$, while the blue histogram shows the offsets for $\langle z \rangle = 2.27$ LBGs from Steidel et al (2010). The arrow shows the shift of 104 km/s measured in the stacked spectrum shown in Figure 6.

be evaluated at the *interaction surface* (also known as Sobolev surface), which is defined (in terms of velocity) by the following equation:

$$v \cos \theta = -c \frac{\Delta(\nu)}{\nu_0}; \quad (1)$$

It is easy to see that this equation defines surfaces of equal projected velocity, at which a photon is processed, for any given observed velocity.

The wind optical depth at the interaction surface, can be written as a function of frequency, wind parameters, and atomic constants, as follows (e.g., ?):

$$\tau(\nu, r) = \frac{\pi e^2}{mc} f_{lu} \lambda_{lu} n_l(r) \left[1 - \frac{n_u g_l}{n_l g_u} \right] \frac{r/v}{1 + \sigma \mu^2}; \quad (2)$$

where $\mu = \cos(\theta)$, $\sigma = \frac{d \ln(\nu)}{d \ln(r)} - 1$, and the values of the atomic parameters can be found in Table ?? . We assume that the wind material follows a truncated velocity law:

$$v = v_0 \left(\frac{r}{R_{SF}} \right)^\gamma \text{ for } r \leq R_W = R_{SF} \left(\frac{v_\infty}{v_0} \right)^{1/\gamma}; \quad (3)$$

$$v = v_\infty \text{ for } r \geq R_W; \quad (4)$$

where v_0 is the wind velocity at the surface of the star-forming region (i.e., at R_{SF}), and v_∞ is the terminal velocity of the wind at R_W . The expression for the optical depth can be simplified by assuming that 1) it does not depend on the angle θ between a radius and a line of sight, 2) the above velocity law holds, and 3) stimulated emission is negligible:

$$\tau = \frac{\pi e^2}{mc} f_{lu} \lambda_{lu} n_l(r) \times \frac{r}{v} \quad (5)$$

The density of ions in the lower level will depend on the gas physical conditions, and in general, can be written as:

$$n_l(r) = E(r) \chi(r) A(r) D n_H \quad (6)$$

where $E(r)$, $\chi(r)$, $A(r)$, and D are the excitation fraction, the ionization fraction, the relative abundance of the element (with respect of H), and the depletion rate; and n_H can be written as:

$$n_H = \frac{\rho(v)}{m_H(1 + 4Y_{He})}, \quad Y_{He} = \frac{n_{He}}{n_H} \quad (7)$$

We focus the attention on [Si II], because we detect multiple transitions both in absorption and in emission.

The density of ions

We neglect photospheric absorption.

we assume that the [Si II] ions trace the neutral phase of the wind around the star-forming regions. However, we should really check this. What if it is in the HII region?.

==¿ outflows a grandi distanze? ==¿ prochaska non trova il transverse proximity effect. ==¿ Ly α nebulae su scale

6.1. Lyman alpha scattering in galaxy outflows

It is frequently noted that Ly α , when found in emission, presents as a feature systematically redshifted from its systemic velocity (Kunth et al 1998, Shapley et al 2003, Tapken et al 2004, McLinden et al 2011). P Cygni-like Ly α profiles are thought to arise by scattering in neutral gas that has been accelerated by mechanical energy returned from the star formation episode (Ahn & Lee XXX, Verhamme et al 2006). Our measured velocity shift for the interstellar absorption lines (150–200 km/s) places our stacked galaxy somewhere in the middle of the distribution for star-forming galaxies in the nearby universe selected for observation with HST (Leitherer et al 2011), suggesting they are not providing extreme feedback compared to their gas masses. Indeed the velocity shift of the LIS absorption lines compared with H α is also very similar to the sample average of 164 km/s measured in LBGs at $z \sim 2.7$ (Steidel et al 2010).

Regarding Ly α emission, radiative transport modeling has suggested that characteristic offsets to Ly α should exceed the blue-shifting of the neutral ISM offsets by factors of around two (Verhamme et al 2008). Measuring neutral ISM lines in faint Ly α -selected high- z galaxies is usually beyond the limits of the data in most LAE spectroscopic observations, but recently a number of Ly α velocity offsets have been measured with respect to H α and [OIII] lines: McLinden et al (2011) report offsets of 125 and 342 km/s for the two galaxies; Finkelstein et al (2011) report a 162 km/s offset in one galaxy and another that is consistent with zero; Hashimoto et al (2012) present four more galaxies with $\Delta v_{Ly\alpha}$ between 0 and 200 km/s; Guaita et al (submitted) present four more galaxies with offsets between 100 and 350 km/s. Our sample of 25 $\langle z \rangle = 0.2$ LAEs is twice the size of the combined samples at $z = 2 - 3$ and find a very similar distribution of Ly α velocity offsets, and suggests this offset to be somewhat characteristic of the Ly α -selected galaxy population, independent of redshift.

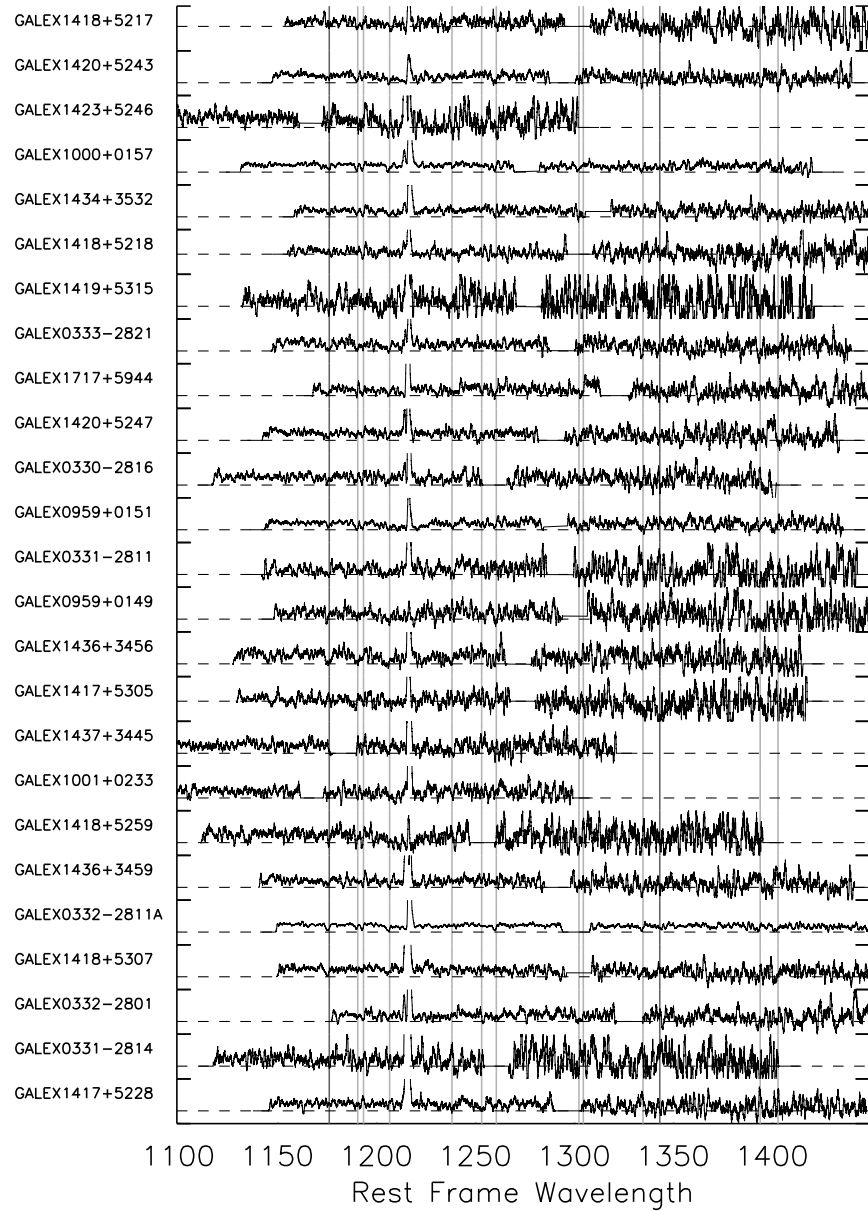


FIG. 5.— Rest-frame full NUV spectra of the 25 sample. The spectra are boxcar smoothed using a box of 1\AA , and are shifted in the vertical direction for clarity. The horizontal dashed lines show the zero flux level corresponding to each galaxy spectrum. Vertical lines mark the wavelength position of some prominent interstellar absorption features.

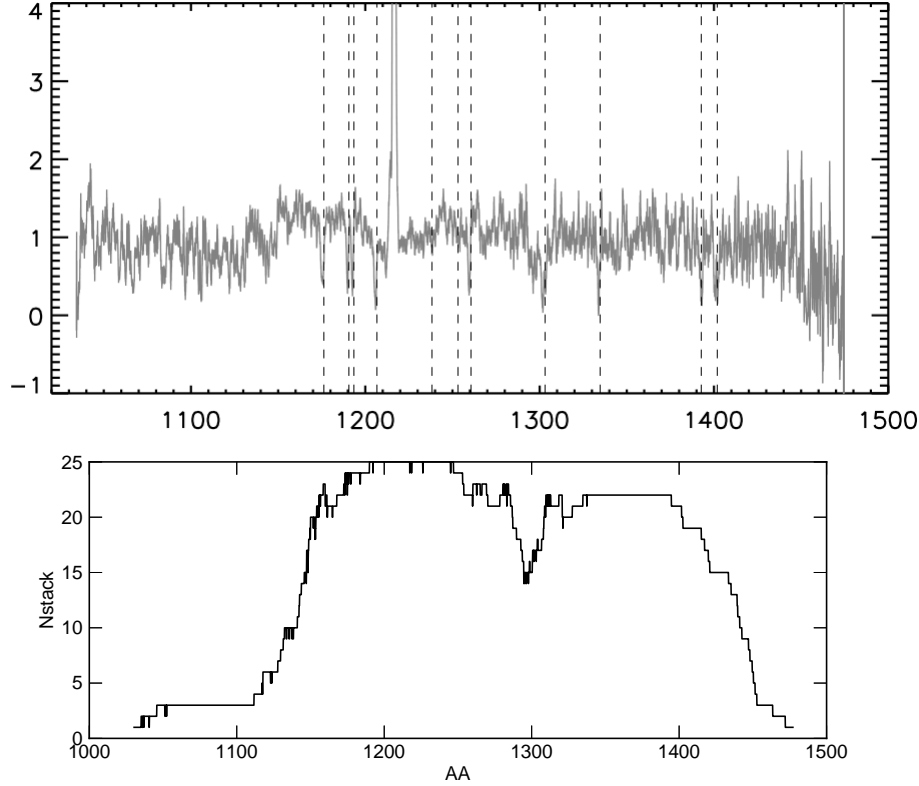


FIG. 6.— Composite spectrum from XXX galaxies. **COULD BE GOOD TO SHOW THE NUMBER OF CONTRIBUTED FRAMES?**

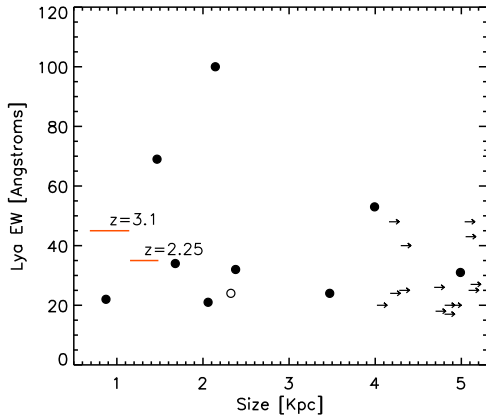


FIG. 7.— $\text{Ly}\alpha$ EW versus UV half light radius. Symbols as in previous figures. Horizontal red bars indicate the range of typical sizes of $\text{Ly}\alpha$ emitters at different redshift as indicated.

Similarly made measurements in continuum-selected galaxies at $z \sim 2.7$ find average absorption line offsets that match that measured in our stacked spectrum with surprising accuracy. It is of marked interest, therefore, that $\text{Ly}\alpha$ -H α offsets measured in the same sample of almost 100 LBGs (Steidel et al 2010, see also Kulas et al 2012) find a an average $\Delta v_{\text{Ly}\alpha}$ four times the value that we measure in the more nearby Universe. While the average offset of $\text{Ly}\alpha$ compared with the LIS lines for LBGs appears consistent with predictions from radiative transport models our average measurement of a $\text{Ly}\alpha$ offset significantly below the LIS offset is in stark contrast to predictions.

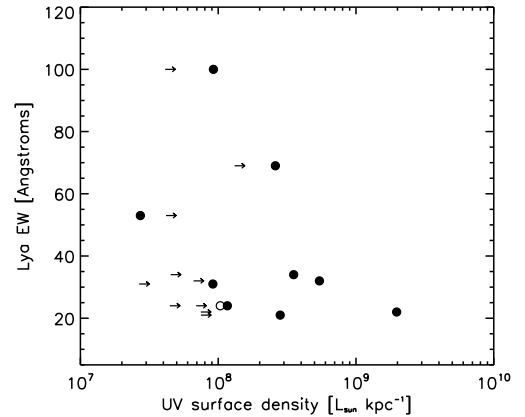


FIG. 8.— $\text{Ly}\alpha$ EW versus UV surface density. Symbols as in previous figures.

A plausible reconciliation of $\text{Ly}\alpha$ shifts below the outflow velocities of the oncoming gas may lie in exactly where in the HI medium $\text{Ly}\alpha$ obtains its redistribution in frequency. A measurement of the LIS lines will return the velocity at which the column density of the absorbing species – and presumably also neutral hydrogen – is highest. For typical column densities in star-forming galaxies this may be on the order of 10^{20} cm^{-2} (Mas-Hesse et al 2003). In static gas, $\text{Ly}\alpha$ becomes optically thick at column densities roughly 6 orders of magnitude below this value, which suggests that the gas responsible for the frequency distribution is both of lower column density and velocity than the bulk of the outflowing gas, and also resides closer to the recombination nebulae. Yet

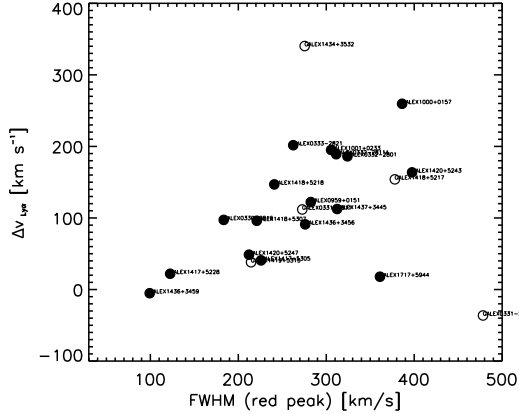


FIG. 9.— The $\text{Ly}\alpha$ - $\text{H}\alpha$ velocity shift compared with the line width of the red peak of the $\text{Ly}\alpha$ profile. Open circles indicates galaxies observed with MIRROR-B.

this scenario is not able to explain the marked difference seen between the $\text{Ly}\alpha$ and UV selected populations: why should the situation be different in the two populations? It is plausible also that we are observing the transition between $\text{Ly}\alpha$ photons that have been backscattered from receding shells (which must acquire around twice the velocity shift of the outflowing gas) and photons that are able to pass directly through the oncoming shell. The multiple peaking of many of the $\text{Ly}\alpha$ profiles is indeed also suggestive of this: indeed it appears that we are observing a large number of double-peaked profiles, in which the red peak is enhanced compared to the blue. From the available publications of transport modeling, this seems most resemblant of photon transfer and frequency redistribution in a single front-side medium.

6.2. What drives the velocity shift?

If the $\text{Ly}\alpha$ velocity shift is present, and the neutral gas observed to be accelerated, then one may expect the feedback to be coupled with other properties of the star-formation episode. Specifically, for example, outflows may be stronger in galaxies of higher SFR or specific SFR which in turn may manifest in larger velocity offsets. Adopting the $\text{H}\alpha$ luminosity as a proxy for SFR and its equivalent width as a rougher proxy for sSFR, we present the $\text{Ly}\alpha$ velocity shift compared with $L(\text{H}\alpha)$ and $EW(\text{H}\alpha)$ in the upper two panels of Figure 10.

The data present no such correlation of offset with SFR. Indeed while higher SFR must imply that more mechanical energy has been fed back to the ISM, it does not necessarily mean that the outflow would be faster. SFR and stellar mass are known to be strongly correlated in almost all galaxy samples, and should the neutral gas mass also scale with stellar mass, proportionally more energy would be needed to drive a superwind of the same velocity. In this picture, a correlation with SFR would not be expected, but one would expect a stronger velocity offset when the SFR per unit mass, or sSFR, increases. Interestingly, then, the plot of $\Delta v(\text{Ly}\alpha)$ against $EW(\text{H}\alpha)$ shows a marked lower envelope consistent with this formulation. Galaxies with low equivalent widths ($\lesssim 100\text{\AA}$) can take the full range of outflow velocities (0 – 200 km/s), whereas galaxies with high sSFR ($EW(\text{H}\alpha) > 200\text{\AA}$: eight of 22 measureable galaxies) present only

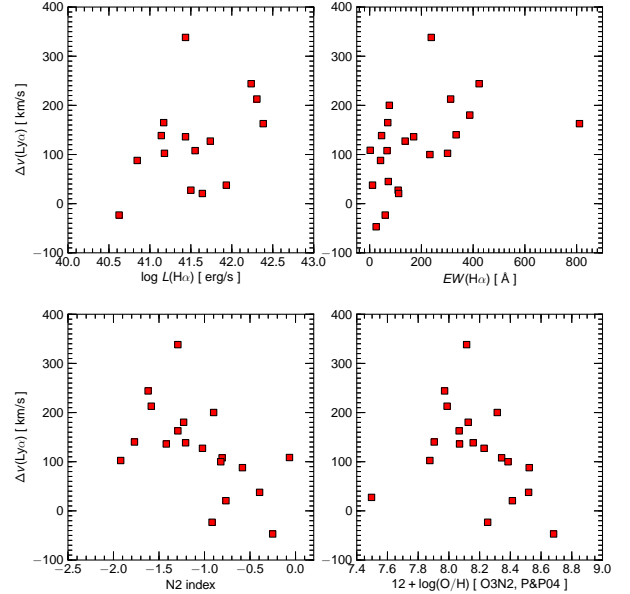


FIG. 10.— The $\text{Ly}\alpha$ - $\text{H}\alpha$ velocity shift compared with (a. *Upper left*) the $\text{H}\alpha$ luminosity; (b. *Upper right*) $\text{H}\alpha$ equivalent width; (c. *Lower left*) N2 index; (d. *Lower right*) gas phase metallicity with $\Delta v(\text{Ly}\alpha)$ above the sample average value of 100 km/s. It is plausible therefore, that since these galaxies have high SFR compared with their stellar mass, their SFRs may also be high compared with their neutral gas mass and are able to push the $\text{Ly}\alpha$ scattering medium to higher velocities.

From the optical spectra we also compute the N2 index $\equiv \log_{10}([\text{NII}]\lambda 6584/\text{H}\alpha)$ and the gas-phase metallicity which we derive from the O3N2 index using the strong line calibration of calibration of (Pettini & Pagel 2004). Here also there appears to be a rough anti-correlation between $\Delta v(\text{Ly}\alpha)$ and N2/O/H. However we note that the emission line measurements involve no quantity sensitive to the mass of the stellar population. Metallicity does, however, correlate strongly with stellar mass, implying that velocity shifts are somewhat higher in lower mass objects. This aligns well with the reasoning presented above, in explaining how a large range of offsets may be observed, despite showing no overall correlation with the total star formation rate.

6.3. How would a neutral Universe effect these observations?

In high-redshift studies, $\text{Ly}\alpha$ fluxes, number counts, luminosity functions, and asymmetries are all thought to be affected by the increasingly neutral fraction of hydrogen in the neutral IGM. However, disentangling possible IGM effects from those of the ISM has never been possible in these galaxy samples. In our $\langle z \rangle = 0.2$ observations we can perform a number of comparison studies on a set of observations for which we can be certain that the IGM has no influence on the $\text{Ly}\alpha$ line. We now proceed to examine how common assumptions about the IGM affect $\text{Ly}\alpha$ photometry and measurements of the profile asymmetry.

6.3.1. Photometry in an ionized and neutral universe

One of the primary use of the $\text{Ly}\alpha$ line in astrophysical cosmology is as a diagnostic of the reionization epoch,

as an increasingly high fraction of intergalactic gas becomes neutral with increasing redshift (Miralda-Escude 1998; Haiman & Spaans 1999; Malhotra & Rhoads 2006; Kashikawa et al. 2006). Furthermore, should one want to derive the intrinsic Ly α output of a galaxy (before IGM attenuation) one needs to correct for the IGM. Indeed frequently, simple prescriptions (e.g. Madau 2005) for the IGM are applied directly to the Ly α line to make this correction (Cassata et al 2011; Blanc et al 2011), which accounts for almost 50% of the Ly α flux at $z = 6$. This is the entire premise for the recent claim of an extremely high EW Ly α emitter at $z = 6.5$ (Kashikawa et al 2012). These corrections include two major unknown questions: by how much is the Ly α line offset redward of its systemic velocity? and how close do the Ly α forest clouds really come to the Ly α line? With these data we have already answered the former question, and we will now proceed with a simple assessment of how common assumptions of the latter may affect conclusions.

Using the systemic redshift for our sample as measured by H α and the canonical prescription for intergalactic Lyman series line blanketing of Madau (1995), we simulate or Ly α spectra in the common redshift windows of $z = 5.7$ and 6.5 . We simply blueshift the galaxies to $z = 0$ and redshift them to the high- z windows, apply the IGM, and re-compute the luminosities using the same method as in Table ?? . We present the luminosities, both unattenuated and suppressed by the $z = 5.7$ and 6.5 IGM, in Table 3, and make a graphical comparison in Figure 11.

Immediately it can be seen that the simulated high- z luminosities lie very close to the total measured fluxes. Only in a handful of cases – obviously the few galaxies with symmetric Ly α lines centred around the systemic velocity – is there a significant suppression of the Ly α line by the IGM. Indeed the majority of Ly α profiles shown in Figure 5 are notably redshifted, with only a small component to the total flux provided by the blue peak. The effect of the IGM is essentially to completely remove the blue peak but leave the redshifted, dominant peak almost completely unaffected. We compute the average values of $L(\text{Ly}\alpha, \text{IGM}) / L(\text{Ly}\alpha, \text{noIGM})$, which evaluates to 0.81 ± 0.17 (standard error on the mean) at both tested redshifts. It is possible that additional flux could be suppressed by the red damping wing of a neutral IGM that has not been accounted for by these models. This would further suppress our Ly α luminosities in the simulated spectra, but it should be noted that this is not usually accounted for either by high- z observational studies. The damping wing would have equal additional effect on high- z data and these simulations. With so many galaxies lying close to the 1:1 line, we find no argument for doubling observed $z \gtrsim 6$ fluxes, especially in individual cases. This conclusion is also supported by the fact that asymmetries do not differ at high- and low- z , as we will discuss in the next section.

6.3.2. Ly α asymmetry in an ionized universe

As well as applying a redward velocity offset to the transferred Ly α line, scattering in neutral gas is also well-known to introduce asymmetries to the profile itself. In the spectra of high- z galaxies, when spectral resolu-

tion permits, Ly α almost ubiquitously presents asymmetrically (Shapley et al 2003; Kurk et al. 2004; Shimasaku et al 2006) and, at the highest redshifts, is expected to be enhanced by neutral gas in the IGM. Indeed, quantitative measurements of the profile asymmetry have also been invoked to discriminate between Ly α emitting galaxies and foreground interlopers (e.g. [OII] emitters where the line is not subject to radiative transport effects; Kashikawa et al 2006). As with the transmitted line flux, however, the effect that the IGM has on the transmitted line is strongly dependent upon how close the IGM comes to the Ly α line that is transported through the ISM.

Our well resolved and high S/N COS observations give us the possibility to compute quantitative asymmetries for a sample of Ly α selected galaxies in which we can say with certainty that the frequency redistribution occurs inside the ISM. We opt to measure profile skewness (Kurk et al 2004), ‘weighted skewness’ (Shimasaku et al 2006) and red/blue ratios of the peak-to-10% wavelength and flux (Rhoads et al 2003). We are able to perform these measurements in 22 of our 25 objects, and present the results in Table 3.

Firstly regarding weighted skewness, the index has been used by Shimasaku et al (2006) at $z = 5.7$ and Kashikawa et al (2006) at $z = 6.5$ to cull interloping galaxies from their sample, by invoking a threshold S_W of > 3 to select LAEs. Scaling our measurements of S_W into the observer frame at these redshifts we present histograms of the S_W for the COS sample in Figure 12. Overplotted are the LAE and low- z samples of Shimasaku, and LAEs measured and compiled in Kashikawa et al. It is immediately clear from these histograms that our GALEX-selected LAEs exhibit a very similar range of S_W to both high- z LAEs samples, whereas the interloping sample of Shimasaku et al (2006) shows very little clear overlap. In order to assess this similarity quantitatively, we employ a K -sample Anderson–Darling (1952) rank sum comparison¹⁰. Indeed for the two LAE samples, data are consistent with the null hypothesis (that the two samples are drawn from the same parent distribution) at only the 28% level ($z = 5.7$) and 69% ($z = 6.5$) level. However the same test performed on the concatenated LAE+interloper sample at $z = 5.7$ suggests there is a $< 3\%$ chance the two samples share the same parent distribution, and the selection of $S_W > 3$ as invoked in those studies seems appropriate. It seems likely, however, that the asymmetry is introduced by the scattering of Ly α photons within the ISM of these galaxies and not by an encroaching neutral IGM. If the IGM does not have an appreciable effect of the asymmetry of the Ly α line at high- z it must reflect the fact that the Ly α forest does not come close enough to Ly α to sufficiently affect the blue wing, possibly because of redshifting within the ISM, which is certainly very consistent with a reduction in flux of only $\sim 20\%$ as shown in the previous Section. If it has an effect at all, it must be very grey, and likely be caused only by the damping wing.

7. CONCLUSIONS

¹⁰ The A–D test is similar to the frequently adopted Kolmogorov–Smirnov (K–S) test but considers the full range of data values as opposed to the largest single deviation, and is therefore more robust against strong biases from outlying points.

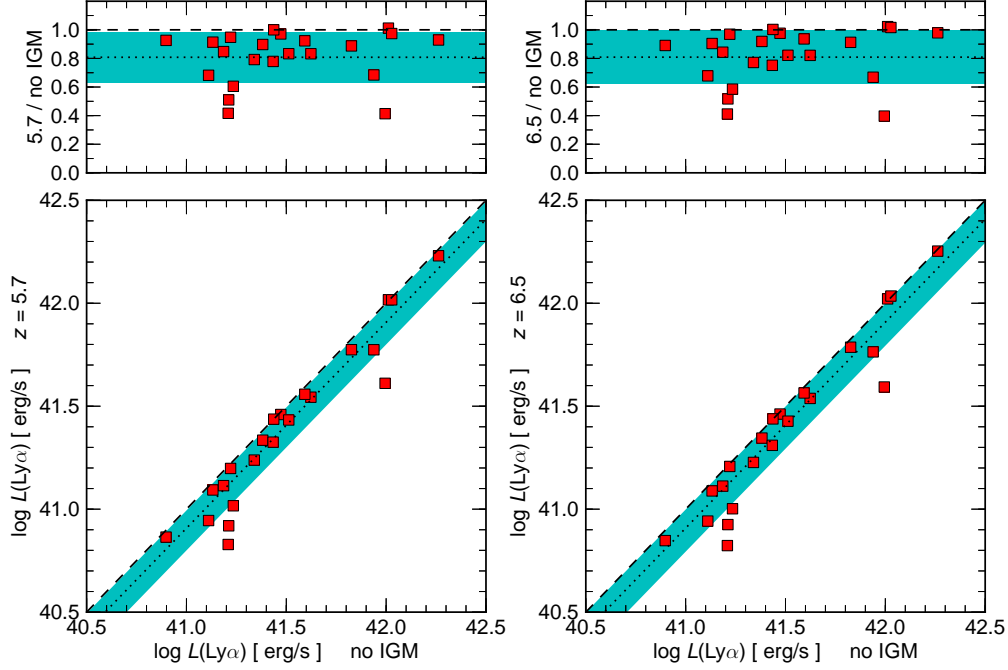


FIG. 11.— Comparison of the measured luminosity of $\text{Ly}\alpha$, with the same measurements when the spectra have been ‘absorbed’ by the standard Madau (1995) IGM prescription assuming redshift $z = 5.7$ (*left*) and $z = 6.5$ (*right*). The lower panels show a direct comparison of the luminosities, while the upper panels show the fractional luminosity that is transmitted through the IGM. By eye the *left* and *right* plots are indistinguishable. The dotted lines show the average ratios of $L_{\{5.7,6.5\}} = 0.81 L(z=0)$, which differ only at the fourth significant digit. Shaded regions show the standard error on the mean, which is almost consistent with the 1:1 line.

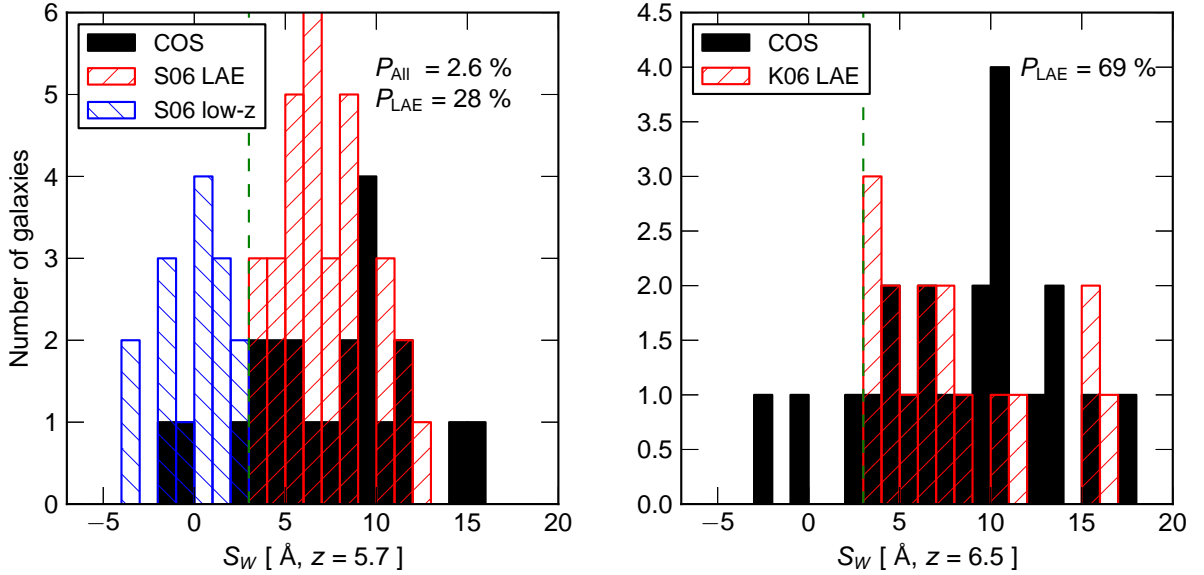


FIG. 12.— Distribution of the weighted skewness S_W of our COS $\text{Ly}\alpha$ profiles. Histograms of our own sample are presented in black, scaled in redshift to $z = 5.7$ (*left*) and 6.5 (*right*). Overplotted in the *left* panel are the LAEs from Shimasaku et al (2006) in red, and the emission line objects determined to be lower redshift interlopers in blue. In the right panel the red histogram shows the LAEs of Kashikawa et al (2006). Labeled in the figures are the probabilities that the high- z samples ($z = 5.7$ LAEs, LAEs+interlopers, and $z = 6.5$ LAEs) are drawn from the same parent population using the K -sample Anderson-Darling rank sum comparison. It shows the LAEs populations to be indistinguishable but LAE+interlopers are clearly unlikely to share an underlying distribution.

REFERENCES

- Atek, H., Kunth, D., Hayes, M., Ostlin, G., Mas-Hesse, J. M. 2008, *A&A*, 488, 491
Atek, H., Kunth, D., Schaerer, D. et al. 2009, *ArXiv e-prints* 0906.5349
Baldwin, J. A., Phillips, M. M., Terlevich, R. 1981, *PASP*, 93, 5
Bruzual, A. G. & Charlot, S. 1993, *ApJ*, 405, 538
Bruzual, G. & Charlot, S. 2003, *MNRAS*, 344, 1000
Caplan, J. & Deharveng, L. 1986, *A&A*, 155, 297

TABLE 2
LY α PROPERTIES

Galaxy	Ly α luminosity	λ_B	λ_R	Morphology	Notes
	$10^{42} \text{ erg s}^{-1}$	\AA			
GALEX1417+5228	1.38 ± 0.03	1467.93 ± 0.01	1469.15 ± 0.01	0	
GALEX0331-2814 ^a	1.30 ± 0.05	...	1556.30 ± 0.10	2	
GALEX0332-2801	0.39 ± 0.02	1475.82 ± 0.01	1478.90 ± 0.01	0	
GALEX1418+5307	0.53 ± 0.02	1462.12 ± 0.01	1463.68 ± 0.03	0	
GALEX0332-2811A	1.06 ± 0.02	...	1465.08 ± 0.01	2	
GALEX1436+3459	0.38 ± 0.02	1473.83 ± 0.01	1474.98 ± 0.01	0	
GALEX1418+5259	0.04 ± 0.02	0	
GALEX1001+0233	1.83 ± 0.14	...	1682.10 ± 0.01	1	
GALEX1437+3445	0.83 ± 0.07	...	1610.23 ± 0.01	1	
GALEX1417+5305	0.31 ± 0.03	...	1541.07 ± 0.01	1	
GALEX1436+3456	0.59 ± 0.04	...	1543.24 ± 0.01	1	
GALEX0959+0149	0.02 ± 0.00	1	
GALEX0331-2811 ^a	0.17 ± 0.01	...	1474.29 ± 0.10	1	
GALEX0959+0151	0.29 ± 0.02	...	1521.75 ± 0.01	2	
GALEX0330-2816	0.52 ± 0.04	1555.92 ± 0.01	1558.40 ± 0.01	2	
GALEX1420+5247	0.40 ± 0.03	1520.95 ± 0.01	1523.22 ± 0.01	0	
GALEX1717+5944	0.24 ± 0.01	...	1453.92 ± 0.01	1	
GALEX0333-2821	0.37 ± 0.03	1515.08 ± 0.01	1517.56 ± 0.01	2	
GALEX1419+5315 ^a	0.25 ± 0.02	1535.93 ± 0.10	1536.80 ± 0.10	1	
GALEX1418+5218	0.22 ± 0.02	...	1507.02 ± 0.01	1	
GALEX1434+3532 ^a	0.16 ± 0.01	1453.15 ± 0.10	1454.12 ± 0.10	2	
GALEX1000+0157	1.23 ± 0.05	1535.20 ± 0.01	1538.83 ± 0.03	2	
GALEX1423+5246	0.36 ± 0.05	1632.31 ± 0.01	1634.03 ± 0.01	0	
GALEX1420+5243	0.11 ± 0.01	...	1517.26 ± 0.01	1	
GALEX1418+5217	0.07 ± 0.01	...	1508.37 ± 0.01	1	

^a Galaxy observed with MIRRORB

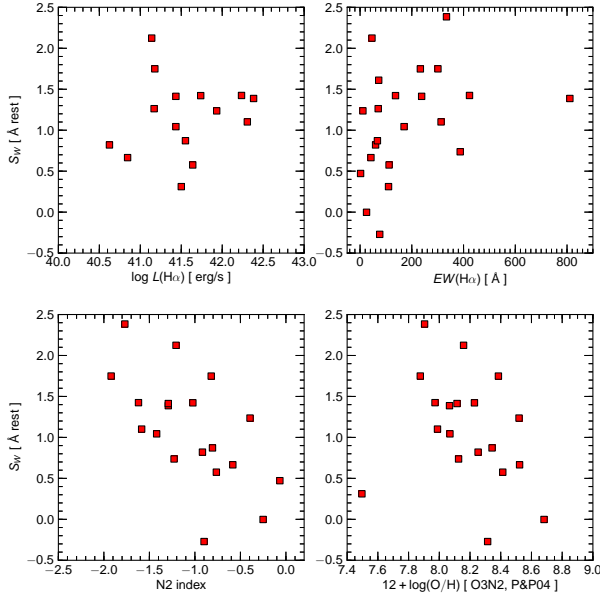


FIG. 13.— Same as Figure 10 but with weighted skewness, S_W .

Cardelli, J. A., Clayton, G. C., Mathis, J. S. 1989, ApJ, 345, 245
Carter, B. J., Fabricant, D. G., Geller, M. J., Kurtz, M. J., &
McLean, B. 2001, ApJ, 559,606

Charlot, S. & Fall, S. M. 1993, ApJ, 415, 580
Cowie, L.L., Barger, A.J., Hu, E.M., 2009, ArXiv e-prints
0909.0031
Deharveng, J.-M., Small, T., Barlow, T. A. et al. 2008, ApJ, 680,
1072
Dijkstra, M., Haiman, Z., & Spaans, M. 2006, ApJ, 649, 14
Finkelstein, S. L., Rohads, J. E., Malhotra, S. et al. 2008, ApJ,
678, 655
Finkelstein, S. L., et al., 2009, ApJ, 700, 276
Finkelstein, S. L., et al., 2009, ApJ, ArXiv e-prints 0906.4554
Gialalisco, M., Koratkar, A., & Calzetti, D. 1996, ApJ, 466, 831
Hansen, M. & Oh, S. P. 2006, MNRAS, 367, 979
Hayes, M. et al. 2007, MNRAS, 382, 1465
Kauffmann, G. et al. 2003, MNRAS, 341, 33
Kewley, L. J. et al. 2001, ApJ, 556, 121
Laursen, P. & Sommer-Larsen, J. 2007, ApJ, 657, L69
Mathis, J. S. 1972, ApJ, 176, 651
Miller, C. J. et al. 2003, ApJ, 597, 142
Natta, A. & Panagia, N. 1984, ApJ, 287, 228
Neufeld, D. A. 1990, ApJ, 350, 216
Neufeld, D. A. 1991, ApJ, 370, L85
Oke, J. B. & Gunn, J. E. 1982, PASP, 94, 586
Ostlin, G. et al. 2008, ArXiv e-prints
Panagia, N. & Ranieri, M. 1973a, A&A, 24, 219
Panagia, N. & Ranieri, M. 1973b, in Les Nebuleuses Planetaires,
275280
Pengelly, R. M. 1964, MNRAS, 127, 145
Valls-Gabaud, D. 1993, ApJ, 419, 7
Verhamme, A., Schaerer, D., & Maselli, A. 2006, A&A, 460, 397
York, D. G. et al. 2000, AJ, 120, 1579

APPENDIX

TABLE 3
LY α PROPERTIES

Galaxy	$L(\text{Ly}\alpha)$ $z \approx 0.2$	$L(\text{Ly}\alpha)$ $z = 5.7$ $10^{42} \text{ erg s}^{-1}$	$L(\text{Ly}\alpha)$ $z = 6.5$	S	S_W restframe Å	a_λ	a_f
GALEX1417+5228	0.8683452	0.59431674	0.58045145	0.3257	0.3111	1.3911	1.1336
GALEX0331-2814	0.9879125	0.40850181	0.39195428	-0.0005	-0.0019	1.1200	1.1664
GALEX0332-2801	0.2968061	0.28822474	0.28972307	0.3302	0.7366	1.4548	1.1182
GALEX1418+5307	0.3253785	0.27104907	0.26745902	0.7069	1.7490	1.9388	1.2733
GALEX0332-2811A	1.0268168	1.03903657	1.04980441	0.7829	2.3841	3.2959	2.5272
GALEX1436+3459	0.1617906	0.06735962	0.06653605	0.2157	0.8201	1.1572	1.0255
GALEX1418+5259
GALEX1001+0233	1.8302378	1.70001528	1.79157804	0.4425	1.1013	1.4782	0.9778
GALEX1437+3445	0.6702077	0.59474476	0.61162917	0.5168	1.4220	1.6727	1.0336
GALEX1417+5305	0.2185427	0.17312553	0.16863250	0.2683	0.6653	1.1339	0.9910
GALEX1436+3456	0.4200032	0.34970323	0.34498662	0.4187	0.8716	1.3015	1.0307
GALEX0959+0149
GALEX0331-2811	0.1290824	0.08804660	0.08752134	0.2148	0.4716	1.2907	1.1101
GALEX0959+0151	0.2410013	0.21624882	0.22142958	0.5152	1.3871	1.5846	0.9668
GALEX0330-2816	0.3915936	0.36145186	0.36668307	0.7417	1.7484	2.3003	1.2957
GALEX1420+5247	0.2715689	0.21156661	0.20416373	0.7195	1.6103	1.7882	1.0904
GALEX1717+5944	0.1627919	0.08300855	0.08414941	0.2319	0.5756	1.2347	0.8833
GALEX0333-2821	0.2735889	0.27358894	0.27433189	-0.1404	-0.2713	0.8893	0.9822
GALEX1419+5315	0.1716515	0.10385135	0.10045273	0.3076	1.2359	1.0930	1.0538
GALEX1418+5218	0.1356059	0.12393059	0.12262569	0.3782	1.0433	1.3154	1.0743
GALEX1434+3532	0.1663425	0.15767323	0.16124933	0.3799	1.4133	1.1025	0.6788
GALEX1000+0157	1.0665986	1.03887225	1.08392759	0.4636	1.4241	1.8650	1.2989
GALEX1423+5246
GALEX1420+5243	0.1534203	0.13006413	0.12941483	0.4176	1.2627	1.6465	1.2509
GALEX1418+5217	0.0789956	0.07316467	0.07035331	0.6654	2.1243	1.6930	1.0659

TABLE 4
ATOMIC DATA FOR Si II ION.

Vac. Wavelength Å	A_{ul} s^{-1}	f_{lu}	$E_l - E_u$ eV	$g_l - g_u$	Lower level Conf., Term, J	Upper level Conf., Term, J
1190.42	6.53×10^8	2.77×10^{-1}	0.0 – 10.41520	2 – 4	$3s^2 3p \ 2P^0 \ 1/2$	$3s 3p^2 \ 2P \ 3/2$
1193.28	2.69×10^9	5.75×10^{-1}	0.0 – 10.39012	2 – 2	$3s^2 3p \ 2P^0 \ 1/2$	$3s 3p^2 \ 2P \ 1/2$
1194.50	3.45×10^9	7.37×10^{-1}	0.035613 – 10.41520	4 – 4	$3s^2 3p \ 2P^0 \ 3/2$	$3s 3p^2 \ 2P \ 3/2$
1197.39	1.40×10^9	1.50×10^{-1}	0.035613 – 10.39012	4 – 2	$3s^2 3p \ 2P^0 \ 3/2$	$3s 3p^2 \ 2P \ 1/2$